Quaternary Geochronology 75 (2023) 101432

Contents lists available at ScienceDirect

Quaternary Geochronology

journal homepage: www.elsevier.com/locate/quageo

Using microcomputed tomography (μCT) to count varves in lake sediment sequences: Application to Lake Sagtjernet, Eastern Norway

Eirik G. Ballo [a,b,*], Manon Bajard [a,b], Eivind Støren [c], Jostein Bakke [c]

[a] Department of Geosciences, University of Oslo, Oslo, Norway
[b] Centre for Earth Evolution and Dynamics (CEED), University of Oslo, Oslo, Norway
[c] Department of Earth Science and Bjerknes Centre for Climate Research, University of Bergen, Norway

ARTICLE INFO

Keywords:
Lake sediments
Varve chronology
Bayesian age modelling
Microcomputed tomography
Geochronology
Holocene

ABSTRACT

Varved lake sediments are one of the most important natural archives that allow annual resolution paleoclimate reconstructions. Conventional varve counting techniques use thin sections to manually identify lamina. However, this technique is destructive, labour intensive and limited to a 2D representation of complex 3D features which may lead to misidentification of varve boundaries. This study presents the use of microcomputed tomography (μCT) scans in constructing varve chronologies, utilizing scanning resolutions of ~50 μm (binned to ~200 μm) for core sections up to 150 cm long. To evaluate this method, we cored and analysed Lake Sagtjernet in Eastern Norway — revealing a 593 cm-long sediment record of the past 10274 ($^{+220}/_{-329}$) years, with continuous laminations from 84 to 533 cm depth (75% of the sediments). Through limnological monitoring and microfacies analyses we demonstrate that the laminations are rare ferrogenic varves, with an annual deposition pattern comprised of seasonal changes in biogenic production superimposed on seasonal precipitates of iron and manganese hydroxides. The floating μCT-counted varve chronology presented here is the first non-glacial varve chronology in Norway and covers 4023 $^{+113}/_{-185}$ years. We find that μCT scans allow for a very fast and non-destructive way of counting varves with sufficient detail of varve boundaries. In the few sections where varve boundaries are too vague to resolve, we recommend using complimentary techniques such as thin sections in parallel. The varve chronology is in good agreement with the 95% confidence interval of the independent radiocarbon chronology based on 16 ^{14}C dates, and ^{210}Pb and ^{137}Cs activity peaks, indicating that the varve chronology can be equated to calendar age.

1. Introduction

From simple quantification of varve chronologies more than 100 years ago (de Geer, 1912), varved sediments have developed into one of the most important natural archives for high-resolution climate reconstructions of the geological past (Ojala et al., 2012; Zolitschka et al., 2015). Increased resolution of analytical scanning methods now allow ultra-high resolution climate reconstructions based on e.g. μXRF (Croudace and Rothwell, 2015) and hyperspectral imaging (Butz et al., 2015). To fully utilize the resolution of these proxy records chronologies of similar resolution is necessary. Due to their annual resolution, varve records have been instrumental in contributing to our understanding of abrupt climate events (Brauer et al., 2008; Rach et al., 2014; Zolitschka et al., 2015), which is key to assess the spatiotemporal trajectories of future climate change.

Reliable varve chronologies are dependent on methods that robustly quantify varves, i.e. varve counting and uncertainty estimation of these counts (Zolitschka et al., 2015). Currently, the most common varve counting approach is manual counting of varve boundaries on digital images of thin sections (Lamoureux, 1994, 2001). However, this technique is time-consuming as it requires intensive laboratory preparation of multiple thin sections — a destructive method which may take months to complete. Furthermore, the thin section plane is limited to a 2D representation of complex 3D features, which may lead to misidentification of varve boundaries (Bendle et al., 2015). Advances in analytical scanning tools now aid in addressing these issues and reduce the time required to produce varve chronologies, while maintaining the accuracy and precision of thin sections.

A powerful tool to overcome the 2D representation of the thin-section is computed tomography (CT) — a series of 2D planar X-ray

* Corresponding author. Post box 1028 Blindern, 0316, Oslo, Norway.
E-mail address: e.g.ballo@geo.uio.no (E.G. Ballo).

https://doi.org/10.1016/j.quageo.2023.101432
Received 8 July 2022; Received in revised form 31 January 2023; Accepted 16 February 2023
Available online 20 February 2023

images, which are processed into a 3D model of density variations within a scanned object (Ketcham and Carlson, 2001; Orsi et al., 1994). Since the development of CT scanners in the 1970s, they have become a standard instrument in hospitals for medical examinations worldwide (Hounsfield, 1973). Following technological advances, a new way of scanning with higher spatial resolution has been introduced, often referred to as microcomputed tomography (μCT). Although there is no formal distinction between medical CT and μCT, the two types of scanners are often distinguished by the latter being able to scan at higher resolutions than 200 μm (Cnudde and Boone, 2013).

Use of medical CT scanners in geosciences goes back two decades (Cnudde and Boone, 2013; Duliu, 1999). However, application on varved sediments includes only a few studies and not using the current highest possible down-core resolutions (Boes et al., 2017; Emmanouilidis et al., 2019, 2020; Fortin et al., 2013, 2019). Recent work by Bendle et al. (2015) used a μCT to scan short (8 cm) sediment subsamples aiming to investigate the potential of μCT scans in recognizing varve structures and comparing them to thin sections. However, the study did not address the use of μCT scans in the production of varve chronologies.

Here, we present the first non-glacial Holocene varve chronology

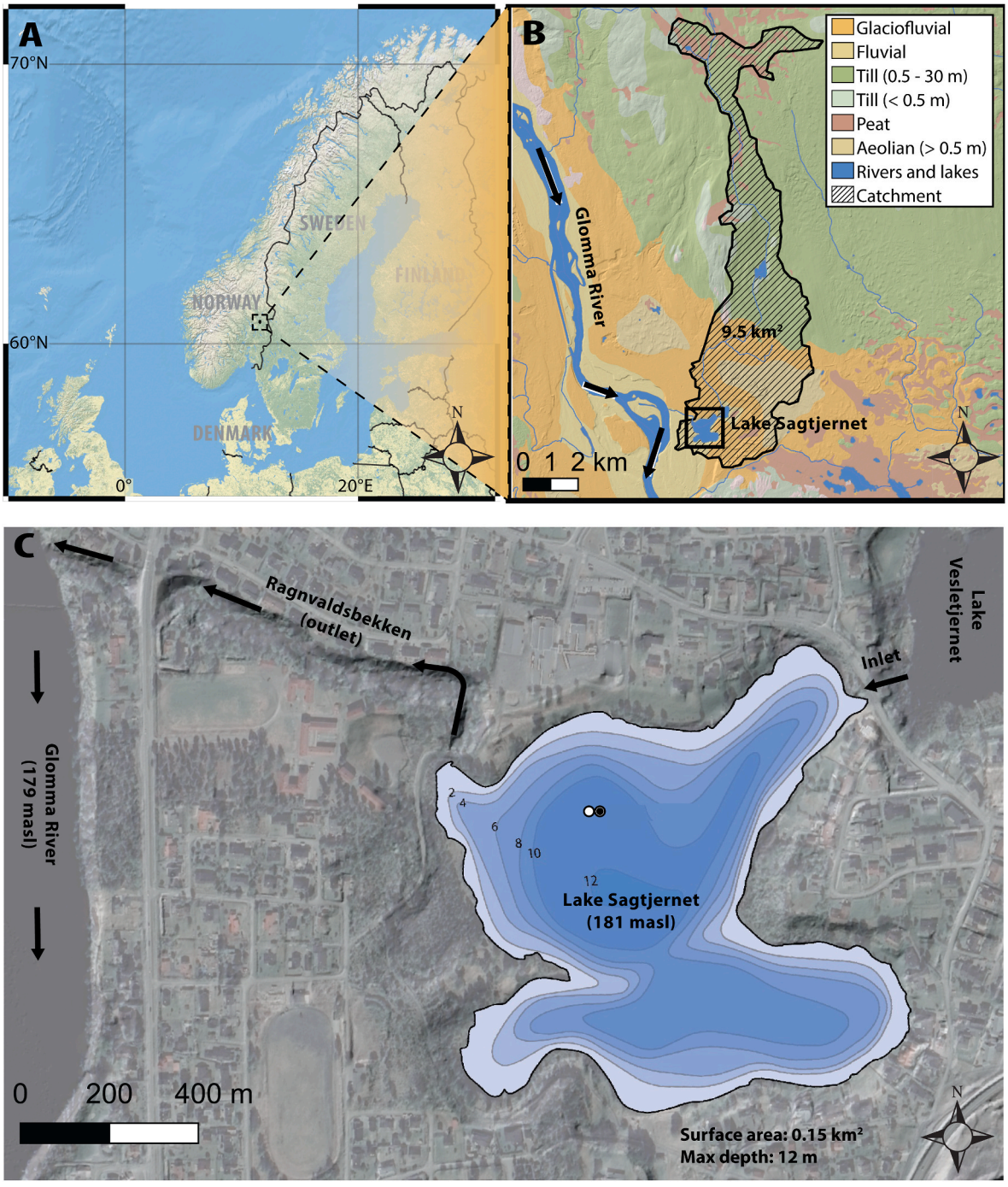

Fig. 1. (A) Map of Northern Europe showing the study site. (B) Map of Quaternary deposits with the Lake Sagtjernet catchment (hashed). (C) Bathymetric map of Lake Sagtjernet showing the coring sites (black and white circles for piston and gravity cores). The immediate surroundings are shown with a hillshade map based on a LiDAR dataset from the national detailed terrain model (NDH) with aerial photograph superimposed. The altitude of Lake Sagtjernet and Glomma River comes from the LiDAR model measured on June 2, 2016 (available from https://hoydedata.no; project name NDH Elverum 5pkt 2016; 5 points/m^2).

from Norway, quantified by varve counting on μCT scans. We cored and analysed Lake Sagtjernet in Eastern Norway, a lake with 593 cm of sediments covering the Holocene period. The varved sediment sequence is quantified using a μCT scanner which can scan up to 150 cm-long sediment cores. To explain how the seasonal sedimentation processes produce laminations in Lake Sagtjernet we combine lake water monitoring,analyses of geochemical sediment properties and analyses of thin sections. Further, we discuss the use of μCT scans to quantify varve chronologies and the related error estimate in the age-depth relationship. Finally, we compare the varve chronology to an independent chronology based on ^{14}C AMS dates and ^{210}Pb and ^{137}Cs activity peaks.

2. Study site

Lake Sagtjernet (*181 masl; 60°53′43″N 11°34′14″E*) is located in the city of Elverum, Norway and has a maximum depth of 12 m and a surface area of 0.15 km^2 (Fig. 1). During the Early Holocene retreat of the Scandinavian Ice Sheet, the Elverum region was flooded by the Nedre Glomsjø glacial-lake outburst flood ~10000–10400 cal. years BP (Hansen et al., 2020; Høgaas and Longva, 2016, 2018; Høgaas et al., 2023). Following the flood, large blocks of ice buried in glaciofluvial material melted to form kettle hole lakes, including Lake Sagtjernet. The total catchment area is 9.5 km^2 and has a low relief (highest point at 416 masl). The main inlet stream continues through till, acidic, humic-rich peat lands and glaciofluvial deposits before entering Lake Vesletjernet, which through a small stream enters Lake Sagtjernet (Fig. 1). The only outlet is through the Ragnvaldsbekken stream into the Glomma River, Norway's largest river (discharge: 720 m^3/s; Fig. 1). The Ragnvaldsbekken stream can be reversed during large flood events of the Glomma River, causing Lake Sagtjernet to receive floodwater and discharge from the Glomma River catchment. This happened during a massive spring flood called "Vesleofsen" in 1995 (Eikenæs et al., 2000). The mean annual air temperature in Elverum is 4.1 °C and annual mean precipitation is 961 mm (Climate-data.org, 2022). Lake Sagtjernet freezes over every winter with an average ice-cover duration of 161 days, and average ice-on and ice-off dates are 16 November and 26 April (2000–2020 average; Table S1).

3. Materials and methods

3.1. Limnological conditions observation

For the duration of one year (2013–2014), we deployed Richard Brancker Research duo loggers (RBR Ltd., Ottawa, Canada) at 2, 6 and 10 m water depth to measure temperature (°C) and dissolved oxygen (DO; mg L^{-1}). Further, we utilized temperature and dissolved oxygen data from the period 1989–1991, which was obtained during a water monitoring project in Lake Sagtjernet named *Sagtjernprosjektet* (Christiansen and Bergaust, 1991). These temperature measurements were measured on water samples using a thermometer. Dissolved oxygen (%) was analysed using the Winkler titration method (Montgomery et al., 1964).

3.2. Coring

The sediment cores were collected from the deepest part of the lake during two coring campaigns in the fall of 2011 and in the fall of 2018 (Fig. 1). Two piston cores (SAGP-211 and SAGP-118) were retrieved using a coring platform and 6 m long 110 mm diameter PVC tubes (Nesje, 1992). To capture the undisturbed sediment-water interface, two additional 1.5 m-long 90 mm diameter sediment cores were collected using a Uwitec gravity corer (SAG-111 and SAG-318). In order to secure safe transport in the field, the long piston cores (SAGP-211 and SAGP-118) were cut into four sections each, while the gravity core SAG-318 was cut into two sections and sealed for transport in vertical position to the Earth Surface Sediment Laboratory (EARTHLAB) at the University of Bergen and stored at 4 °C. Before opening, the SAGP-118 and SAG-318 core sections were scanned in the μCT scanner. Then, all core sections were split lengthwise in the lab, visually described, depth scales were established, and a visual log was drawn before further analysis.

3.3. μCT scanning

The SAGP-118 and SAG-318 core sections were scanned unopened in a vertical position in a ProCon CT-ALPHA CORE system in January 2020. The custom-built scanner located at EARTHLAB, University of Bergen (Norway) was specifically designed to scan sediment cores. The scanner can scan core sections up to 150 cm long with a 240 kV microfocus X-Ray source and a 9 MP detector. Scanning parameters were set to optimize the contrast in density variations through the core. The helix scans of the two SAG-318 gravity core sections (90 cm diameter) were scanned with identical instrument settings: a tube voltage of 110 kV, 850 μA current, and a 334 ms exposure time, resulting in a voxel (volumetric pixel) size of 45.5 μm. All the four SAGP-118 piston core sections (110 cm diameter) were scanned using identical instrument settings: a tube voltage of 120 kV, 800 μA current, and a 267 ms exposure time, resulting in a voxel size of 53.0 μm. Due to the high computational demand when analysing the μCT data, each voxel was binned four times, resulting in a voxel resolution of ~200 μm (further discussed in section 5.3). Processing, visualization and analysis was accomplished using Thermo Scientific Avizo software (version 9.1.1).

3.4. μXRF geochemistry

All core sections were scanned on an ITRAX (XRF) core scanner from COX Analytics at EARTHLAB at 0.2 mm resolution in February 2020. The sediment surface was cleaned and smoothed before being covered by an ultra-thin plastic film to avoid contamination and drying of the sediment during scanning. The μXRF scanning parameters were optimized to detect Fe, Mn, Ca, Si, Ti and K. These settings were set to a voltage of 22 kV (28 kV for the top SAG-318 core section) and a current of 22 mA (28 mA for both SAG-318 core sections) for 10 s with a Mo tube. We calculated the log incoherent (inc)/coherent (coh) scattering ratio, a common proxy for organic matter in lake sediments (Liu et al., 2013; Woodward and Gadd, 2019).

3.5. Thin section preparation and analyses

To better understand the seasonal depositional cycle in Lake Sagtjernet, we prepared four thin sections for mapping of the geochemical composition of the different lamina in February 2020. These four thin sections were evenly spread across the depth of the sediment sequence to ensure that potential changes in the seasonal dynamics over time would be identified. Sediment intervals were cut at depths 132.9–142.9 cm, 244.2–254.2 cm, 297.9–308.9 cm and 525.3–535.3 cm, using plastic U-channels (10 × 2 × 1.5 cm). The U-channels were then frozen using liquid nitrogen, freeze-dried for 48 h and, finally, impregnated under a vacuum with two-component epoxy (EpoFix) for complete impregnation. The resulting blocks of sediments were then cut, glued on a glass slide, and polished to get 25-30 μm-thick thin sections. We investigated the composition and structure of each sub-lamination by producing multiple Energy Dispersive Spectroscopy (EDS) elemental maps using a Hitachi SU5000 FE-SEM with a Dual Bruker Quantax XFlash 30 EDS system at the Department of Geosciences, University of Oslo. Using an acceleration voltage of 15 kV with an 80x magnification yielded a resolution of 1890 pixels for these EDS elemental maps. Individual point analysis used an acceleration voltage of 15 kV.

3.6. Counting laminations and estimating uncertainty

Laminations were counted on exported images from the μCT scans.

μCT scanning of the six core sections (SAG-318; 2 and SAGP-118; 4) resulted in six 3D density reconstruction models of up to 150 cm lengths (Fig. 2A). From each of these six 3D models we first exported one 2D cross section from the centre of each core section, as there is less sedimentary deformation from coring along the centre line. The μXRF scan was also completed along the same line (section 3.4). Each of the six cross sections were first counted once using the CooRecorder software (https://www.cybis.se/forfun/dendro/). Instead of performing multiple counts on the same set of cross sections, we took advantage of the 3D representation that μCT scans provide by exporting another set of six cross sections from the 3D μCT models to perform a second count (Fig. 2B).

To estimate count uncertainty, we identified *marker horizons* (i.e., individual laminations) that confidently could be correlated across the two 2D μCT cross sections (Fig. 2B). Lamination count uncertainties were calculated individually for each *count interval* (i.e. the sediment sections between marker horizons) and then applied to every lamination within that count interval (Fig. 2C). Positive (over-counting) and negative (under-counting) uncertainty was calculated based on the difference between the two counts in each count interval. If count 1 is greater than count 2, it is considered a positive uncertainty and the positive uncertainty is increased by the difference between the two counts. If count 2 is greater than count 1, it is considered a negative uncertainty and the negative uncertainty is increased by the difference between the two counts. The positive and negative uncertainty can then be expressed per count interval (e.g. +5) or as a cumulative uncertainty (e.g. $^{+3}/_{-4}$) where uncertainties from all count intervals above a selected lamination is compiled. This method of expressing uncertainties is adapted from Boes et al. (2017) and Vandergoes et al. (2018), but is modified to express positive and negative uncertainties. Each of the count intervals were also assigned a varve quality index (VQI; Lotter and Lemcke, 1999) between 3 and 0, based on how well the μCT scans capture lamination boundaries (3 = outstanding preservation, 2 = good preservation, 1 = poor preservation, 0 = not distinguishable).

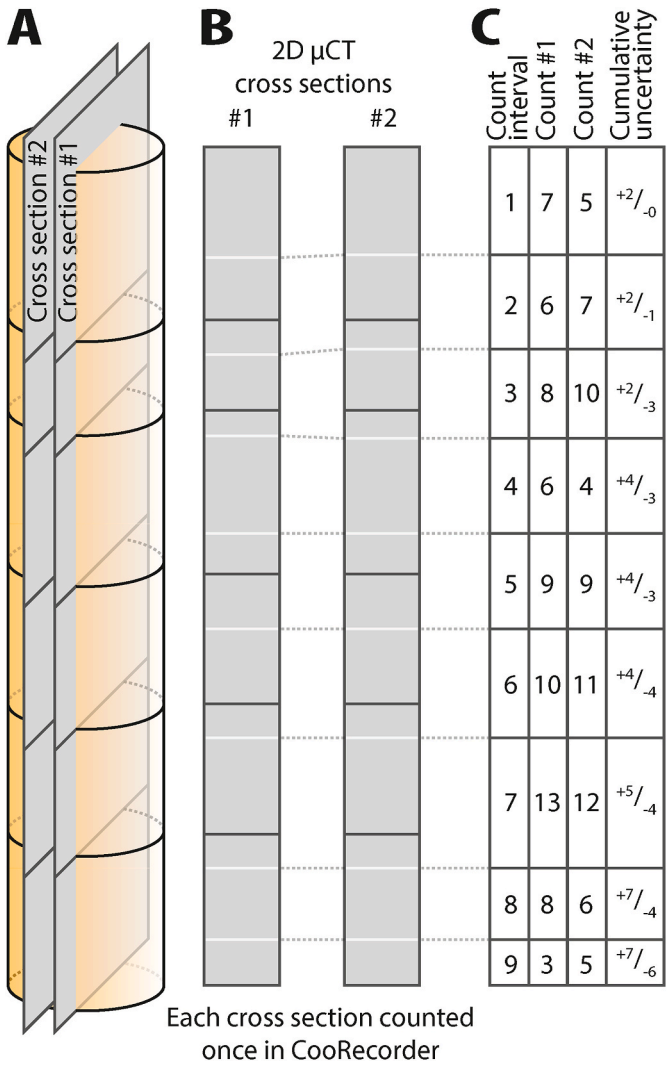

Fig. 2. Conceptual sketch showing how we used μCT data to count varves and estimate uncertainties. (A) 3D μCT model illustrated as an orange composite core containing six cylindrical core sections. Two composite 2D μCT cross sections cut the centre of the 3D μCT model. (B) Two composite 2D μCT cross sections exported from the 3D μCT models constructed from six individual exports each. White lines represent marker horizons that can be correlated across the two 2D μCT cross sections. (C) Conceptual table showing how uncertainties are estimated for each counted interval.

3.7. Independent dating methods

To evaluate the lamina-counted chronology, we built an independent age-depth model based on 16 Accelerator Mass Spectrometer (AMS) radiocarbon dates on plant macro remains. For the upper part, the chronology is based on analyses of short-lived radionuclide measurements (^{210}Pb and ^{137}Cs). AMS measurements were done at Poznan Radiocarbon Laboratory, Beta Analytic and Radiocarbon laboratory at Uppsala University. The dates were calibrated to calendar years before 1950 CE (cal. years BP) using the package *Bacon* (v. 2.4.0) in "R" (Blaauw and Christen, 2011) and the IntCal20 calibration curve (Ramsey et al., 2020).

To measure ^{210}Pb and ^{137}Cs activities we continuously sampled the top 20 cm of the SAG-111 core with 1 cm intervals. The samples were analysed in the Liverpool University Environmental Radioactivity Laboratory by gamma spectroscopy, using Ortec HPGe GWL series, well-type coaxial low background intrinsic Ge detectors (Appleby, 1986). ^{210}Pb was determined via its gamma emissions at 46.5 keV, and ^{226}Ra by the 295 keV and 352 keV γ-rays emitted by its daughter isotope ^{214}Pb following 3 weeks of storage in sealed containers to allow radioactive equilibration. ^{137}Cs and ^{241}Am were measured by their emissions at 662 keV and 59.5 keV, respectively. The absolute efficiencies of the detectors were determined using calibrated sources and sediment samples of known activities. Corrections were made for the effect of self-absorption of low energy γ-rays within the sample (Appleby et al., 1992).

4. Results

4.1. Limnological monitoring of Lake Sagtjernet

The temperature measurements show that Lake Sagtjernet is thermally stratified between March and November and inversely stratified from November to March (Fig. 3C). The deepest part of the lake (10–12 m) holds a stable temperature with an annual mean temperature of 5.5 °C, with the highest temperature of 5.6 °C (January 16, 2014) and the lowest temperature of 5.4 °C (July 4, 2013; Fig. 3C). In mid-September 2013 the thermocline begins to weaken, and the lake becomes isothermal in the second half of October 2013 (Fig. 3C). The lake freezes over on November 26, 2013 (10 days after the 2000–2020 mean ice-on date). In 2013–2014 the ice cover lasts for 133 days, which is 28 days shorter than average (161 days/~5 months). Half the ice-cover has melted on April 8, 2014 (the entire ice-cover is gone by April 13, 2014), 20 days before the 2000–2020 mean. Throughout the measurement period, the oxic-anoxic boundary (1 mg L^{-1}) ranges between 6 and 7 m depth, leaving the deep waters of Lake Sagtjernet anoxic throughout the year — a typical feature for meromictic lakes (Fig. 3D). Fall mixing of the upper mixed zone starts in early September 2013, mixing down to a depth of 5–6 m. As the lake freezes over, wind-driven circulation is restricted. Just a few days after the lake ice melts, partial spring mixing

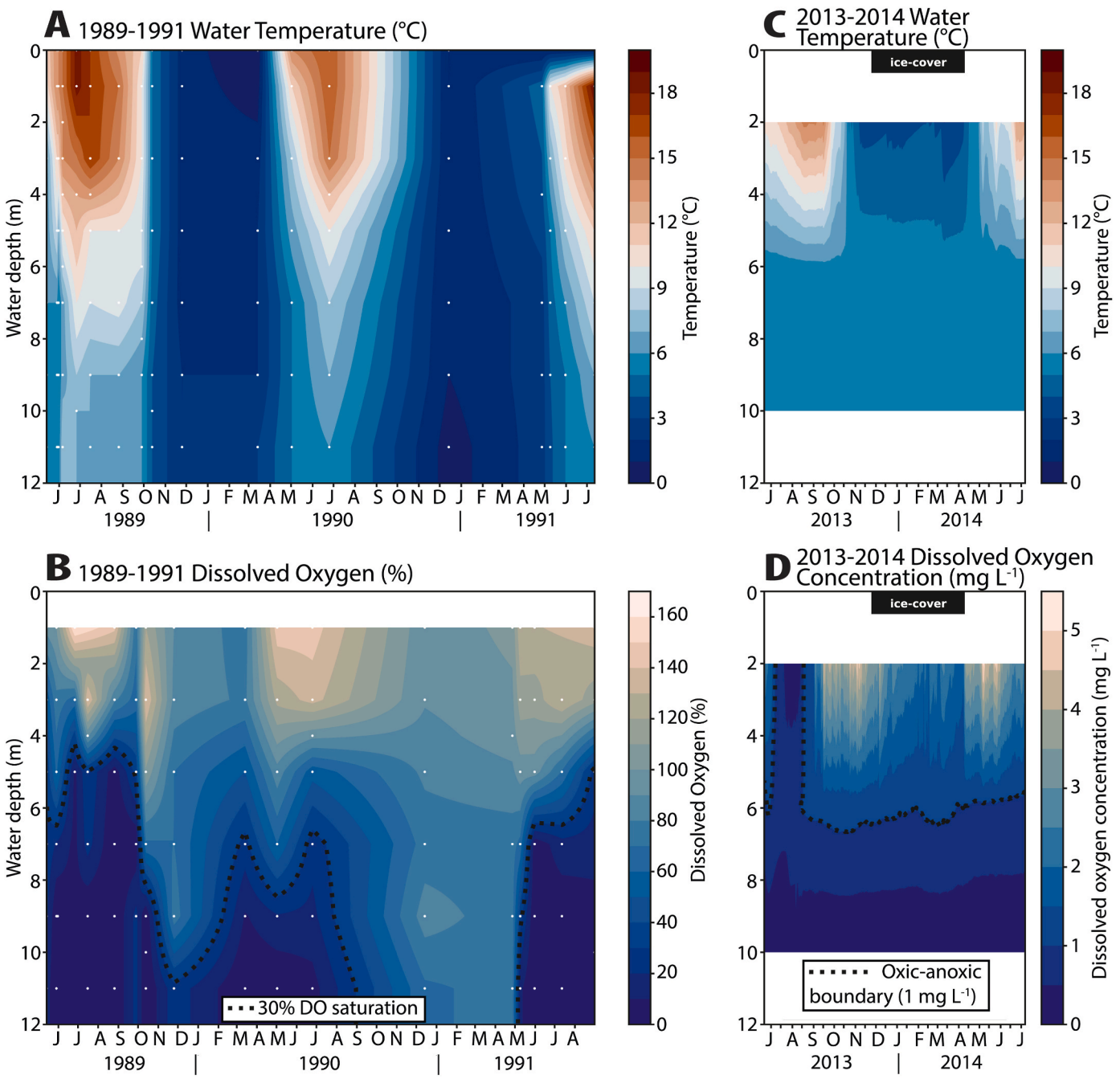

Fig. 3. Lake Sagtjernet depth profiles of temperature and oxygen through two measurement periods. (A) Temperature (°C) from May 1989 to August 1991. The data comes from *Sagtjernprosjektet* (Christiansen and Bergaust, 1991) and is comprised of 18 separate measurement dates shown as white dots. Temperatures have been interpolated between measurement points. (B) Dissolved oxygen (DO; %) from May 1989 to August 1991. Oxygen levels between these measurement dates have been interpolated to produce this plot and must therefore be interpreted with caution. (C) Temperature (°C) daily means from June 2013 to July 2014. (D) Dissolved oxygen (DO; mg L^{-1}) daily means from June 2013 to July 2014. The horizontal black bar shows the ice cover period. The ice cover periods for 1989–1991 are unknown.

starts (Fig. 3C). Oxygen concentrations in the upper mixed zone decline from late-May and into the summer months — the highest oxygen concentration through the year at 2 m depth occurs on May 7, 2014 (5.10 mg L^{-1}), while the lowest occurs on July 30, 2013 (0.17 mg L^{-1}). The annual mean oxygen concentration at 2 m depth is 2.67 mg L^{-1}.

During the period 1989–1991 the temperature evolution portrays a normal signal for lakes in this region: warm surface waters through the summer months (JJA mean; 16.6 °C) and ice-cover through the winter months (Fig. 3A). The bottom waters hold an annual mean temperature of 4.8 °C. Oxygen measurements show complete mixing during the spring of 1989 and the fall of 1990 (Fig. 3B). The measurements also show that the lake only experiences partial mixing during the spring of 1990. By May 29, 1990, the bottom waters quickly become anoxic from 9 m and down. A complete mixing occurs during the fall, and a mild winter enables the mixing to continue for a prolonged period. Following the spring mixing in 1991 the bottom waters of the lake quickly become anoxic again. Fe measurements taken during the spring and summer of 1989 indicate very high levels of Fe in the bottom waters of the lake (Fig. S2).

4.2. Lithology

Generally, sediment colour changes from deep brown/black in the basal part of the core, through light beige/olive in the middle section to rust brown in the upper part of the core. Based on visual logging the sediments were subdivided into four main lithological units (Units D, C, B and A) from the bottom to the top of the sequence (Fig. 4).

Unit D (593–580 cm). The basal part of the unit consists of grey coarse silt (593-591 cm), overlaid by a layer of dark grey clay (591-590 cm) followed by dark homogenous organic sediments (590-588 cm). Above this, there is another layer of grey coarse silt to sandy sediments (588-580 cm). There are no laminations in this unit.

Unit C (580–533 cm). The unit consists of coarse deep brown/black, 'dry' homogenous organic sediments abundant in macrofossils (e.g. leaves and tiny twigs). A light grey 1 cm thick clay deposit is present at 578 cm depth. Two thin (<1 cm) silt deposits are also present in the unit at 574 and 552 cm, which consist of clay and silt and are found as distinct peaks in Ti (692 and 254 cps). Throughout the unit, Fe and Mn concentrations are the lowest (Unit C mean: 13472 and 157 cps) found in the entire core (Fig. 4). The transition to Unit B is sharp.

Unit B (533–84 cm). Sediment colour ranges between light beige, olive-brown and deep brown/black (e.g. Figs. 5.2, 5.3 and 5.4). The

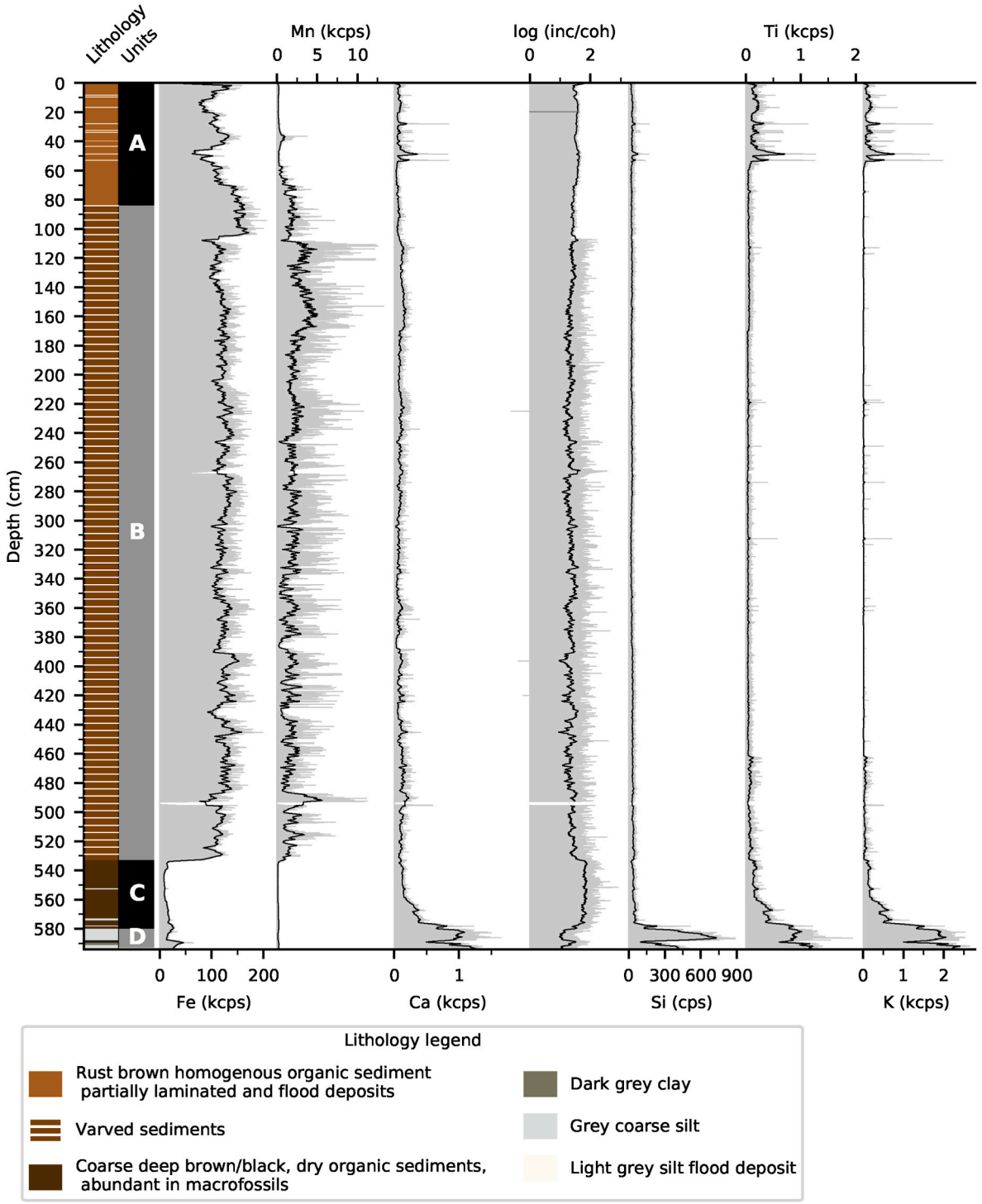

Fig. 4. Core lithology, units and μXRF data (5 cm running mean overlaid).

sediments are fine-grained homogenous organic, which differs from the organic sediments in Unit C. The geochemical properties vary with the colours of the sediments: the lightest coloured sections of the core show elevated values of Fe and Mn and high contrast in the µCT scans, while the deep brown/black sections are characterized by low values of Fe and Mn and low contrast in the µCT scans (e.g. Figs. 5.3 and 5.4). The entire unit is laminated. The laminations consist of thin ~1 mm thick light beige and deep brown/black couplets.

Unit A (84–0 cm). A rust brown colour dominates the unit. The main lithology is homogenous organic sediments/gyttja with high water content, making the sediments incohesive and 'soupy'. Several thin (~1 mm) light grey layers are present in the unit: the three most visible occur at depths 53, 49 and 28 cm (Ti: 1253, 1257, 1123 cps). Another 7 light grey layers are present, though somewhat thinner, at 43, 40, 34, 33, 17,

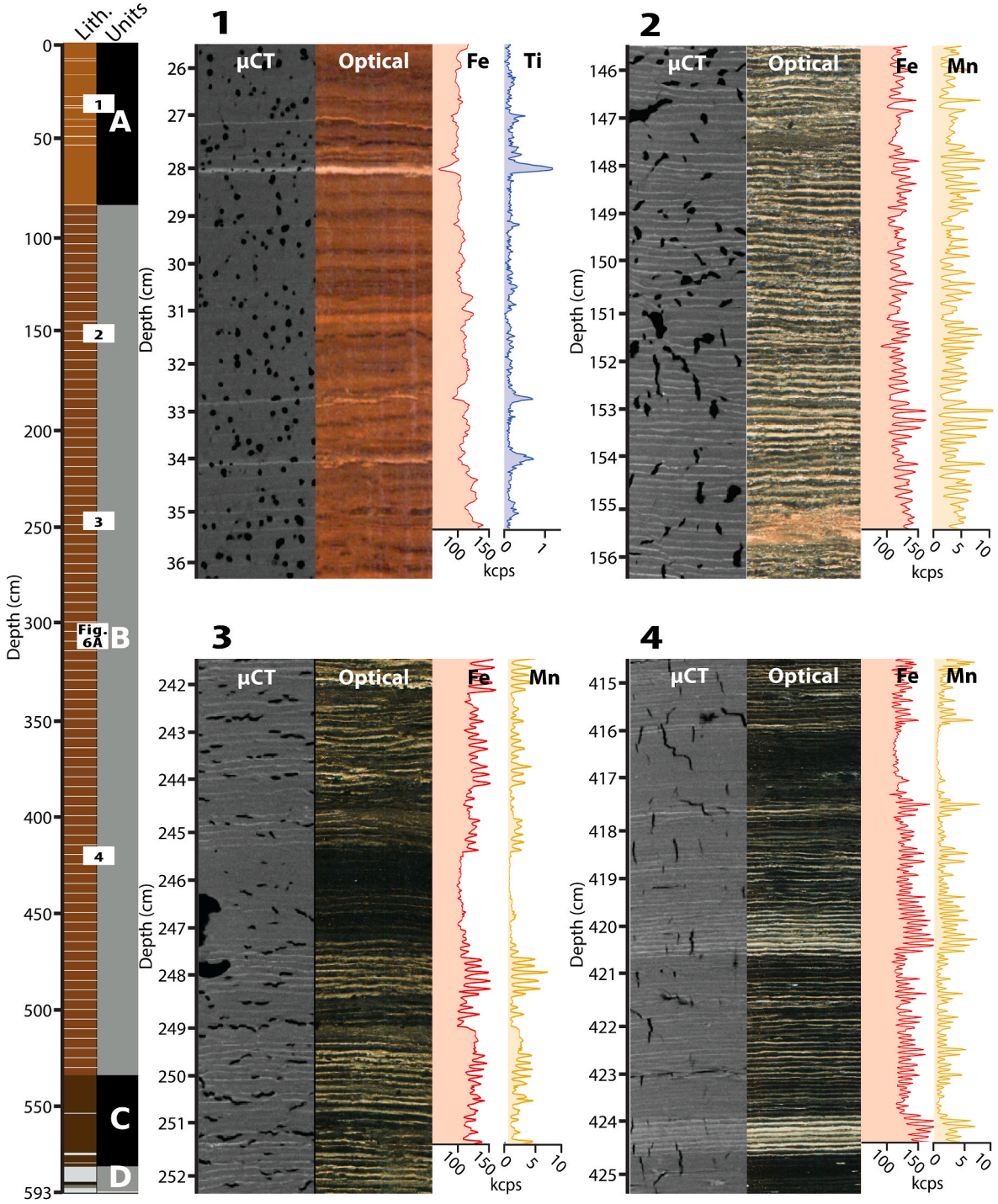

Fig. 5. Examples of sedimentological characteristics (µCT, optical image, µXRF) at four different depth intervals in Lake Sagtjernet. Left: core overview showing lithology and sedimentary units with the position of each of the four examples (white textboxes). (1) 26–36 cm depth: laminations can be observed in the optical image, but are not captured in the µCT image. Three flood layers indicated by peaks in Ti and bright, high density layers in the µCT image. (2) 146–156 cm depth: a common representation of the laminations in Lake Sagtjernet where light layers are characterized by peaks in Fe and Mn. (3) 242–252 cm depth: a 2 cm black band observed in the optical image (~245–247 cm depth) is characterized by decrease in Fe and Mn and lower contrast between lamina in the µCT image. (4) 415–425 cm depth: two black bands (~416–417 and ~425 cm depth) characterized by decrease in Fe and Mn and lower contrast between lamina in the µCT image.

10 and 8 cm. All these light grey layers are characterized by peaks in Ti (351, 638, 656, 666, 484, 309, 118 cps) as well as high ('bright') density in the μCT output (Fig. 5.1). Peaks in Ca, Si and K are also present at these layers. The unit is largely laminated, however, varve boundaries are difficult to distinguish both by visual logging as well as in the μCT scans (Fig. 5.1).

4.3. Lamination microfacies

To identify the common depositional pattern of the laminations, we analysed four thin sections of sediments using a scanning electron microscope (SEM; section 3.5 and Fig. 6B). Two major sub-lamina define the typical alternation of sedimentation: (1) a thinner pale lamina composed of Fe and Mn hydroxide colloids, and (2) a thicker darker lamina composed of amorphous organic matter (Fig. 6B). This pattern seen in the SEM imaging is further reflected in the μXRF scans, which show Fe and Mn maxima corresponding to the pale-coloured lamina (Fig. 6A). Furthermore, the μXRF scans show small regular Ca maxima correlating to Fe and Mn maxima. The pale-coloured lamina are in the μXRF scans characterized by minima in the log (inc/coh) scattering ratio, indicating less organic matter (Fig. 6A). Common indicators for minerogenic detritus such as Si, Ti and K show very low values in the μXRF scans and their maxima are irregular (Fig. 6A). The μCT scan images capture the colloidal metal lamina as denser (brighter, higher greyscale values) while the biogenic lamina are captured as less dense (darker, lower greyscale values; Fig. 6A). In the thin sections, some of the colloidal metal lamina appear to be split into two separate sections (Fig. 6B).

4.4. μCT scanning

Based on μCT scanning it was possible to construct volumetric 3D models of a total of 6 sediment core sections from Lake Sagtjernet, all of which are shown with a spatial resolution of ~200 μm. The core sections were examined individually both in 3D using *volume rendering* as well as 2D cross sections using the *orthoslice* function in the Avizo software (Fig. 7). The output data is presented as greyscale values that represent the attenuation of X-ray energy passing through the sample to the recording detector. Greyscale values form a frequency distribution where the densest parts of the sediments have the highest (brightest) greyscale values and the least dense have the lowest (darkest) greyscale values. As the scanning parameters were adjusted for each scanned core section, greyscale values cannot be directly correlated between core sections. All scanned core sections contain considerable amounts of gas bubbles, represented as low (darker) greyscale values (Fig. 7). The presence of gas bubbles did not prove to be a significant problem in this study.

In the μCT output, laminations are represented as alternating layers of relatively high (brighter) and low (darker) greyscale value corresponding to Fe and Mn-rich deposits (high) and organic deposits (low), respectively (Figs. 5 and 6). The resolution of lamination boundaries decreases down the core, likely due to compaction of the sediments and reduction of water in the pore space. Although laminations can be observed visually in Unit A (0–84 cm), they are practically undetectable in μCT scans (Fig. 5.1).

4.5. Lamination counting

During the first master counting we identified a total of 275 marker horizons (section 3.6) resulting in 274 count intervals (all in lithology Unit B). The mean number of laminations contained in each count interval is 15, while the lowest and highest number of laminations counted in one interval is 1 and 122, respectively. A total of 4023 laminations were counted along 449 cm in the sediment profile (Fig. 8). We counted laminations from 84 cm depth, where lamination boundaries became clear enough to follow continuously, down to 533 cm depth. The cumulative count error at the bottom of the laminated counted sequence is $^{+113}/_{-185}$ laminations (Fig. 8). The average VQI of the counted interval is 2.1, indicating that the majority of the counted laminations are well preserved. Mean lamination thickness for the entire study interval is 1.12 mm with a consistent down-core decrease. Mean lamination thickness for the top and bottom 100 cm is 1.67 mm and 0.73 mm, respectively.

4.6. Radiocarbon dating and age-depth modelling

A total 17 radiocarbon samples were analysed (Table 1 and section 3.7). Among the 17 samples, one was excluded from the age-depth model (Beta-343461 at 44.8 cm depth), as it is clearly too old when compared to the other radiocarbon dates and most likely resedimented (Fig. 8). The base of the sediment core is dated immediately below the boundary between Unit D and C (581.8 cm) by a small bark fragment (Poz-47269) as well as aquatic moss (Poz-47270) producing ages of 10242–10653 and 9789–10367 cal years BP, respectively. All samples were inspected by a botanist prior to analyses to ensure a terrestrial origin, however, one sample (Poz-47270) was analysed despite being identified as aquatic moss. The younger age of the aquatic moss compared to the terrestrial bark fragment at the same depth indicate that there is no hard water effect in Sagtjernet. As all the other the other samples are terrestrial we assume that they incorporate carbon in equilibrium with the atmosphere, which is also reflected in the $\delta^{13}C$ values of the samples.

The ^{137}Cs activity shows two relatively well-defined peaks, at 1.25 cm and 4.25 cm depths in SAG-111 (Supplementary Data). A peak in ^{241}Am concentrations coinciding with the 4.25 cm ^{137}Cs peak can be interpreted as the maximum atmospheric production of ^{137}Cs from the 1963 CE atmospheric testing of nuclear weapons (Appleby et al., 1991). The more recent ^{137}Cs peak (1.25 cm) appears to record fallout from the 1986 Chernobyl accident. Extrapolating the ^{137}Cs chronology to the surface of the core, the date of uppermost sediments of the SAG-111 core is calculated to be 1996 ± 2 years, with the most recent 15 years of deposition likely lost during coring, possibly caused by a diffuse water-sediment boundary. Total ^{210}Pb activity reaches equilibrium with the supporting ^{226}Ra at a depth of around 12 cm in the SAG-111 core and unsupported ^{210}Pb concentrations decline with depth, suggesting relatively uniform accumulation (Supplementary Data). Ages calculated using the ^{210}Pb CRS dating model (Appleby and Oldfield, 1978) are given in detail in the Supplementary Data. The ^{137}Cs and ^{210}Pb dates were incorporated into the Bacon model alongside the ^{14}C dates, to generate the age-depth model presented in Fig. 8.

According to this age-depth model the sedimentation rate is relatively low, but consistent, from 533 to 593 cm (Unit D and C), with a mean of 0.09 mm year^{-1}. The age-depth model clearly shows one major change in sedimentation rate at 533 cm depth, which corresponds to the lithological transition from Unit C to Unit B and onset of laminations — dated to 4548 $^{+132}/_{-117}$ cal years BP (Fig. 8). Above the onset of laminations the sedimentation rate abruptly increases more than tenfold to a mean of 1.15 mm year^{-1} (533-0 cm; Units B and A). The mean sedimentation rate for the entire lamination counted sequence is 1.12 mm year^{-1} (Unit B).

5. Discussion

The sediments in Lake Sagtjernet contain continuous laminations from 84 cm to 533 cm depth (75% of the sediment core; Figs. 4 and 8). Here we discuss if these laminations can be characterized as varves (i.e., formed annually) by first evaluating the lake monitoring data and the seasonal cycle in water temperature and oxygen concentrations. Second, we discuss if the sedimentation pattern and formation of lamina can be tied to the annual cycle of the lake. We then evaluate how μCT scans perform as a tool to count varves. Finally, we compare the varve count chronology towards the independent radiocarbon age-depth model.

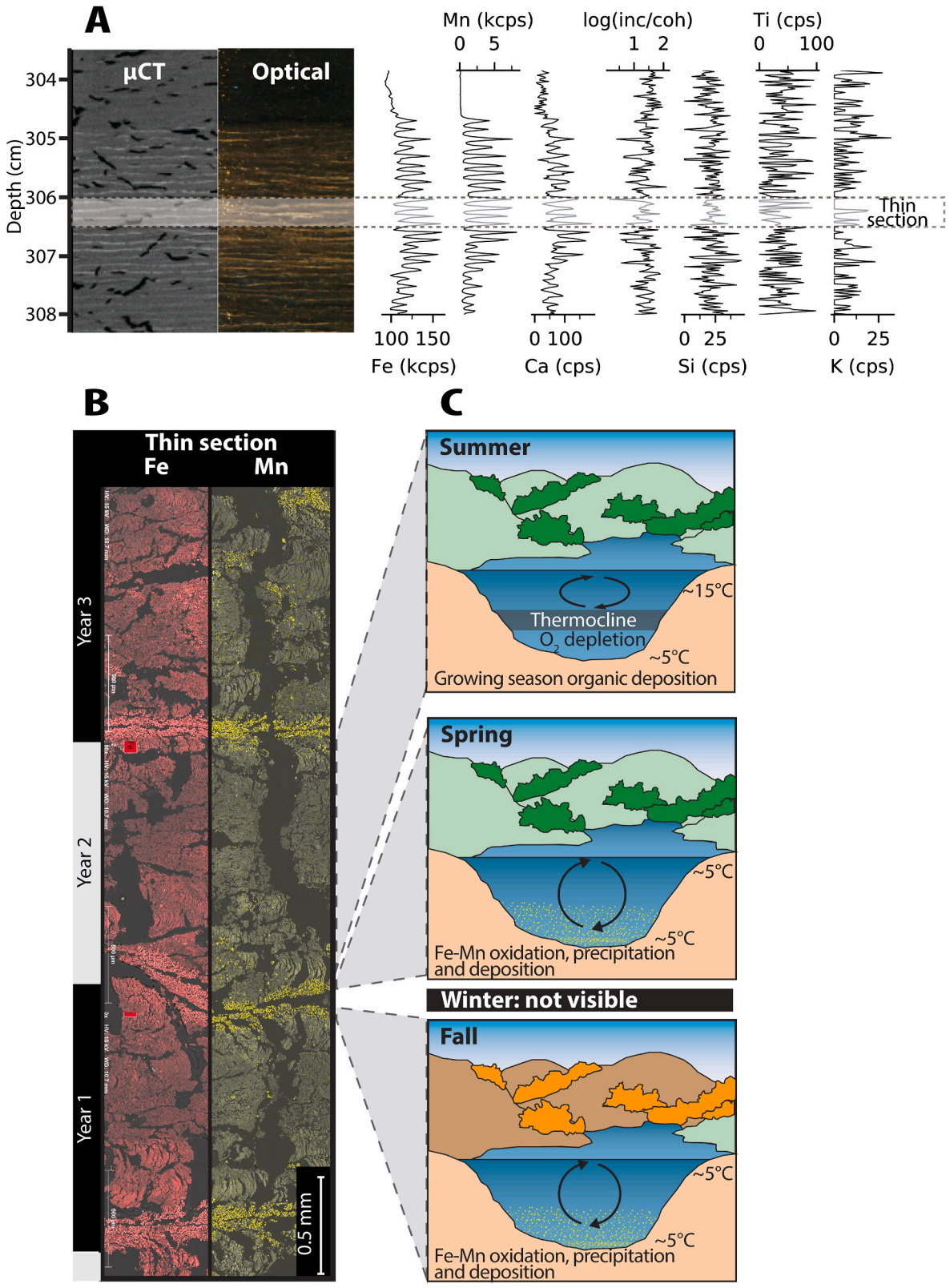

Fig. 6. Scheme detailing varve formation mechanisms in Lake Sagtjernet. (A) µCT cross section image, optical scanning image and µXRF scanning data for Fe, Mn, Ca, Si, Ti, K and log (inc/coh). (B) Thin section SEM elemental map of Fe and Mn across three varve years highlighting the spring/fall colloid deposition. (C) Seasonal limnologic settings associated with the deposition of each lamina.

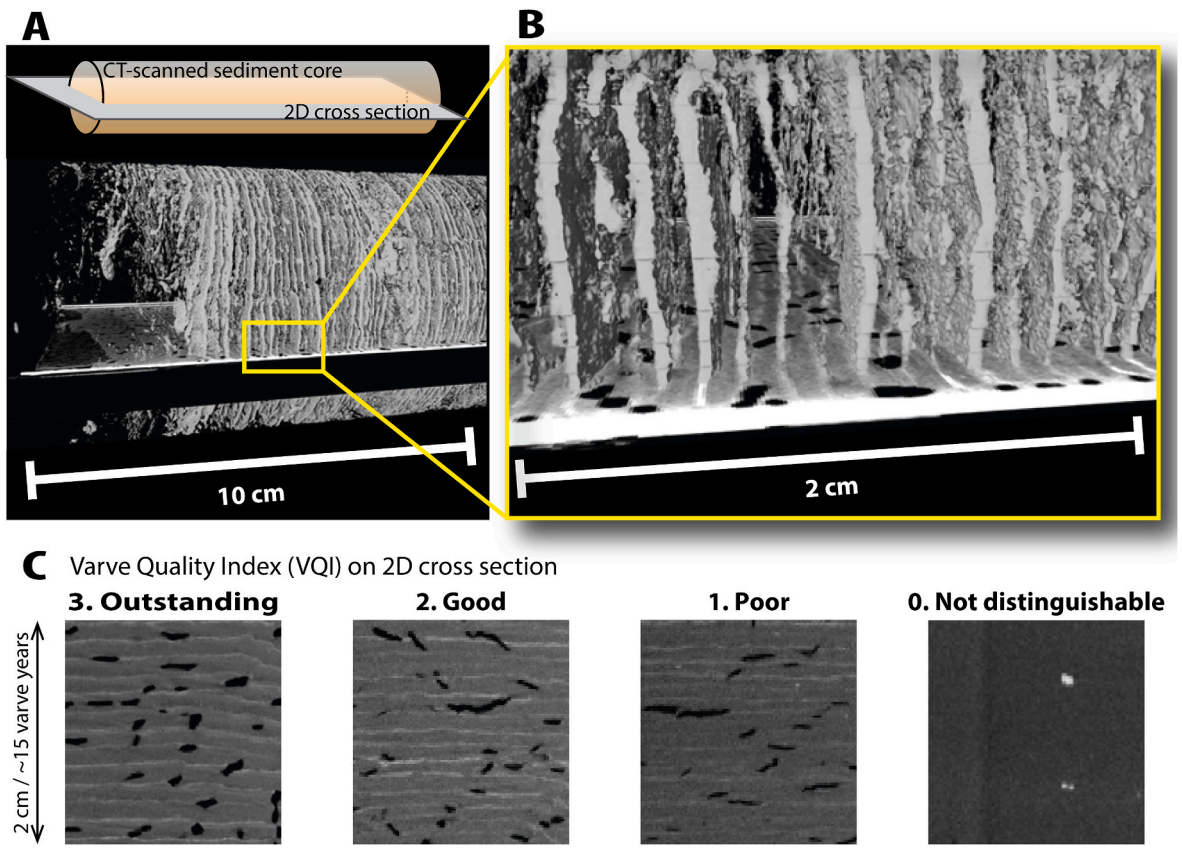

Fig. 7. μCT images illustrating the output of (A) volumetric 3D rendering with a 2D cross section going through the Lake Sagtjernet sediment core at ~1200 cal. years BP, (B) magnification of the 3D rendered section, and (C) varve quality index (VQI) shown on 2D cross section images. The greyscale values reveal the relative density of the sediments, with the bright colour being the densest. In the 3D rendering in (A) and (B), the lowest density sedimentary lamina (growing season organic deposition) has been filtered out to allow visual representation of the spatial relationships of the higher density, metal-rich laminations.

5.1. Limnological conditions for varve formation

The 1989–1991 monitoring data shows multiple mixing regimes through the measurement period (Fig. 3B). Incomplete overturning occurs during fall 1989 and spring 1990. Complete overturning occurs during fall 1990 and spring 1991 (Fig. 3B). In fall 2013, Lake Sagtjernet becomes isothermal in mid-October (Fig. 3C), which in many temperate lakes leads to complete wind-driven fall overturning (Denys, 2009). However, the oxygen measurements show an incomplete fall overturn — the oxic-anoxic boundary only reaches a water depth of ~6 m (Fig. 3D). An incomplete spring overturn is again observed following the outbreak from winter ice in 2014 (Fig. 3D). The lake is therefore in a meromictic phase during the 2013–2014 measurement period. The monitoring data through these two periods (1989–1991 and 2013–2014) indicate that the lake may experience three different mixing regimes as part of the annual cycle:

1. Dimictic conditions with complete overturn twice a year;
2. Monomictic conditions with complete fall overturn and incomplete spring overturn. Poor aeration of the water column during the spring circulation has been shown to be a common feature for lakes in Eastern Norway (Hongve, 1980, 1997) with similar characteristics as Lake Sagtjernet (area <0.3 km^2 and max depth >10 m);
3. Meromictic conditions caused by two consecutive incomplete seasonal turnover events. This is usually caused by an enrichment of dissolved substances in bottom waters, or persistent temperature gradients. The region of Eastern Norway is known for a rich occurrence of meromictic lakes (Hongve, 2002; Kjensmo, 1968; Swanner et al., 2020).

Common for all these mixing regimes is that Lake Sagtjernet remains strongly stratified and anoxic in the bottom-waters during the majority of the year — creating ideal conditions for deposition and preservation of varves.

5.2. Annual sediment deposition cycle

As outlined in section 4.3, the thin section microfacies analyses reveal a rhythmic deposition of two major sub-lamina: a thinner pale lamina composed of iron and manganese hydroxide colloids, and a thicker darker lamina composed of amorphous organic matter (Fig. 6B). The sediment cycle in Lake Sagtjernet appears to be very similar to the sediment cycle described by Anthony (1977) from Lake of the Clouds (Minnesota, USA). This cyclical deposition of iron and manganese is seen in the Lake Sagtjernet μXRF data (Figs. 4 and 5) and is relatively stable through the entire section of laminated sediments (Unit B; Fig. 4). Based on the limnological monitoring data and the resulting geochemical composition of the sediments we argue that the laminations in Lake Sagtjernet are formed annually through the following seasonal depositional mechanisms:

Fall. As the lake becomes isothermal, wind-driven overturning lowers the oxic-anoxic boundary (Fig. 6C). This causes the high concentrations of dissolved Fe and Mn in the deeper waters of Lake Sagtjernet to precipitate into colloidal Fe and Mn hydroxides which in turn are deposited on the lake floor (Davison and Tipping, 1984; Gunnars et al., 2002). Small amounts of Ca are likely adsorbed by the hydroxides as they precipitate (Fig. 6A; Davison, 1993). The chemical composition of the lamina shows high accumulation of Fe and Mn and is in the μCT images seen as a light, high-density lamina (Figs. 5 and 6). Furthermore, the reduction of the log (inc/coh) scattering ratio (Fig. 6A) suggests a

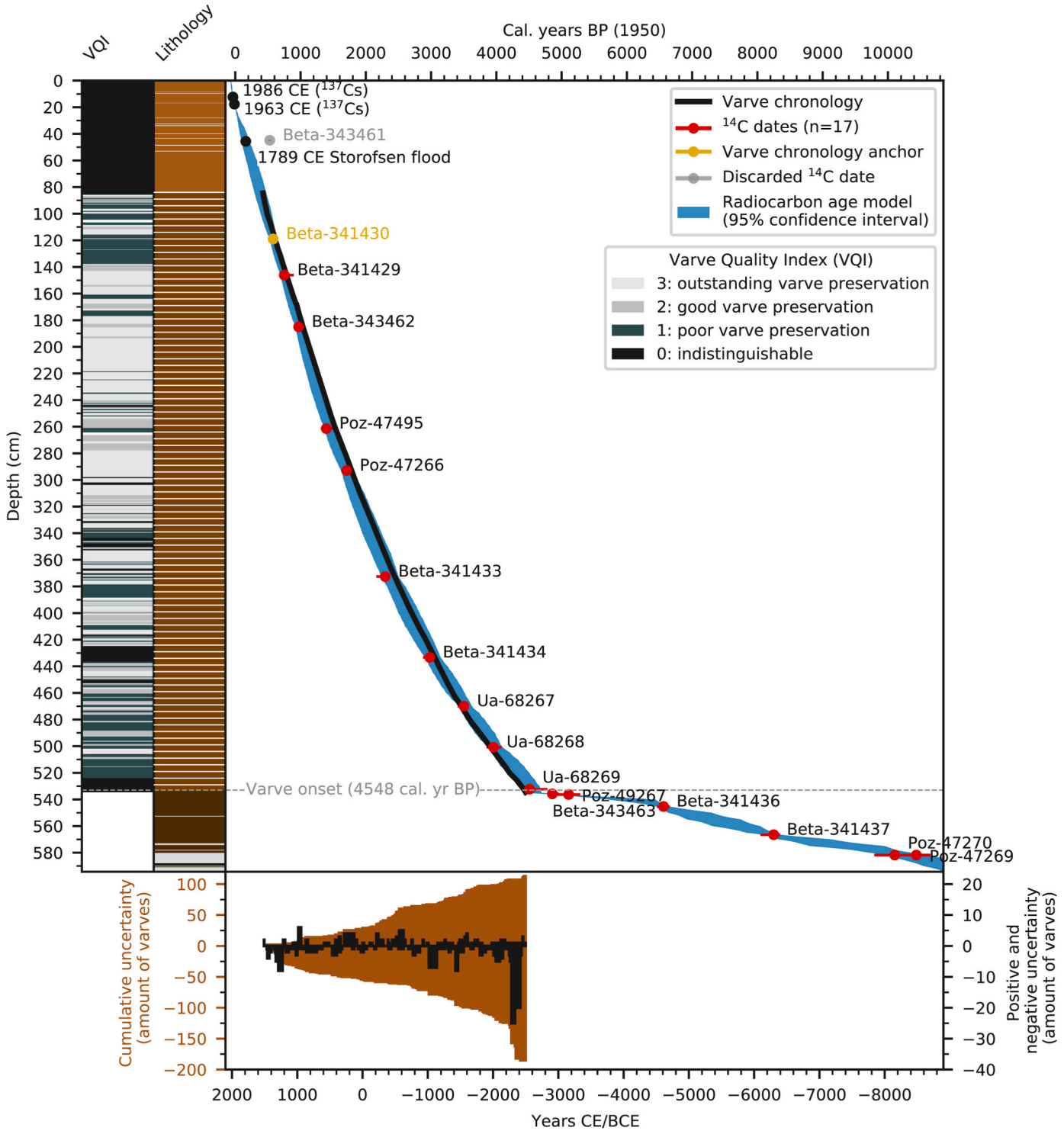

Fig. 8. Lake Sagtjernet age-depth models. Left: VQI and lithology. Right: Age-depth models: the black line is the master varve count chronology, the blue plot is the 95% confidence interval of the Bacon radiocarbon age-depth model. Calibrated age uncertainties of each ^{14}C date are expressed by asymmetrical red error bars. Lower: Distribution of varve count uncertainties: cumulative positive and negative uncertainty for the entire sequence (brown) and positive and negative uncertainty per count interval (black).

decrease in deposition of organic matter in this lamina (Zolitschka et al., 2022).

Winter. Lake Sagtjernet is commonly ice covered from November through April and only experiences low autochthonous primary production. This is shown in the sediments as a thin black lamina (<0.2 mm), as quantified in the thin section (Fig. 6B). The μCT images show that the lamina is only visible in the top ~50 cm of the sediments, however, as we move down-core, it disappears and makes the fall and spring lamina appear as one merged lamina (Fig. 6B). A similar pattern was shown by Anthony (1977) for Lake of the Clouds (Minnesota, USA) where the top decimetres of the varves show thin dark winter lamina separating the fall and spring Fe hydroxide deposits, which disappear down-core. This down-core disappearance in both lakes may be explained by compaction.

Table 1
Macrofossils dated with the AMS radiocarbon method. The calibrated dates were calculated according to the IntCal20 curve (Reimer et al., 2020).

Lab ID	Depth (cm)	Material	δ^{13C} (‰ VPDB)	C^{14} age BP	Calibrated date BP (95.4%)	Calibrated mean date BP (cal. years BP)	Lab
Beta-343461[a]	44.8	Terrestrial plant macrofossil	−29.1	500 ± 30	500–551	527	Beta Analytic
Beta-341430	119.0	Terrestrial plant macrofossil	−27.3	560 ± 30	523–639	579	Beta Analytic
Beta-341429	146.1	Terrestrial plant macrofossil	−25.3	850 ± 30	684–896	750	Beta Analytic
Beta-343462	185.0	Terrestrial plant macrofossil	−26.8	1060 ± 30	920–1056	970	Beta Analytic
Poz-47495	261.4	Terrestrial plant macrofossil	−23.2	1515 ± 35	1310–1515	1394	Poznan
Poz-47266	292.9	Terrestrial plant macrofossil	−22.1	1815 ± 30	1621–1821	1707	Poznan
Beta-341433	372.6	Terrestrial plant macrofossil	−23.9	2300 ± 30	2160–2358	2297	Beta Analytic
Beta-341434	433.3	Terrestrial plant macrofossil	−23.9	2860 ± 30	2876–3071	2979	Beta Analytic
Ua-68267	470.0	Piece of leaf	−28.0	3284 ± 34	3406–3574	3504	Uppsala
Ua-68268	500.8	Piece of leaf	−26.8	3636 ± 30	3849–4081	3956	Uppsala
Ua-68269	532.3	Piece of leaf	−27.0	4035 ± 36	4416–4784	4507	Uppsala
Beta-343463	535.8	Terrestrial plant macrofossil	−24.4	4290 ± 30	4825–4960	4858	Beta Analytic
Poz-49267	536.3	Terrestrial plant macrofossil	−28.8	4450 ± 35	4884–5286	5108	Poznan
Beta-341436	545.3	Terrestrial plant macrofossil	−22.6	5760 ± 30	6458–6656	6561	Beta Analytic
Beta-341437	566.5	Terrestrial plant macrofossil	−28.3	7410 ± 40	8046–8347	8249	Beta Analytic
Poz-47269	581.8	Bark fragment	−43.8	9260 ± 80	10242–10653	10435	Poznan
Poz-47270	581.8	Aquatic moss	−39.0	9000 ± 80	9789–10367	10104	Poznan

[a] Dates discarded from Bayesian age-depth modelling.

Spring. The spring lamina follows the same depositional processes as the fall, given that the spring turnover is complete. However, incomplete or missing spring mixing is quite common to many small inland lakes in Norway, especially in years with long winters (Hongve, 2002). Due to the missing winter lamina in Lake Sagtjernet, it is difficult to discriminate fall and spring lamina from each other (Fig. 6).

Summer. Increased solar insolation during the spring leads to the start of the algal bloom, which is large throughout the summer months and dominated by blue-green algae (Anabaena sp.) as well as Dinobryon sp. And Volvox sp. (Christiansen and Bergaust, 1991). This internal production leads to deposition of the amorphous organic lamina (Fig. 6B), which is further reflected as maxima in the log (inc/coh) scattering ratio in μXRF scans of the sediments. Strong thermal stratification of the water column leads to anoxia in the hypolimnion and thus little precipitation of Fe hydroxides to the lake floor.

Elements Si, Ti and K constitute some of the most important indicators for detrital minerogenic input. In Lake Sagtjernet, however, these elements show very low μXRF values and their maxima cannot be fixed to any season (Fig. 6A). The low μXRF values of Si, Ti and K is further supported by an absence of mineral grains in the SEM imaging, which suggests that the lake receives very little detrital minerogenic input through a normal year of deposition.

Overall, we conclude that despite three different mixing regimes through the monitoring period, the laminated sediments of Lake Sagtjernet reflect an annual pattern with seasonal changes in biogenic production superimposed on seasonal precipitates of Fe and Mn hydroxides. The annual structure of the sediment deposition is captured in both the μXRF data (mainly by the negative correlation between Fe–Mn and log (inc/coh) scattering ratio) as well as the μCT scans (Figs. 4–6). Varves of this type are commonly called ferrogenic (i.e. Fe-rich) and are classified as biogenic-endogenic varves (Zolitschka et al., 2015). Ferrogenic varves, sometimes also called siderite varves (e.g. Wittkop et al., 2014), are known from Holocene lake sediments (Renberg, 1981), however, they are not as common as other types of varves (e.g. clastic-biogenic varves). Ferrogenic varves develop in lakes rich in soluble Fe(II) where seasonal mixing of the lake leads to redox changes which controls the precipitation of the less soluble, oxidized Fe(III) (Davison, 1993; Davison and Tipping, 1984; Gunnars et al., 2002; Mortimer, 1941). Previous studies show that high concentrations of Fe in the groundwater surrounding Lake Sagtjernet are well-known (Kalskin and Hilmo, 1999; Oppistov, 2019; Papadimitrakis, 2019), indicating that there is a natural source of Fe within the lake catchment that can replenish the Fe in the lake water.

5.3. Quantification of varves using μCT scanning techniques

This study shows the potential of using μCT scans to count varves as a faster alternative to counting on thin sections. Unopened core sections require no preparation before being placed in the μCT scanner, with the scanner itself only needing ~1 h for setup, ~7 h of scanning, and ~4 h for rebuilding the scanned files. Therefore, a 150 cm-long, unopened core section can be ready to be counted in *CooRecorder* just one day after returning from the field.

Optimizing the μCT scanning resolution for each core section is a priority, however, as with any analytical technique there are compromises to be made. As described in section 3.3, we scanned the 150 cm-long core sections at the smallest possible voxel sizes for 90 and 110 mm diameter cores: 45.5 and 53.0 μm. van der Bilt et al. (2021) showed that it is possible to scan at even higher resolutions (~20 μm) by extracting 2–3 cm wide U-channels from the sediment cores, as the reduced diameter of the scanned object minimizes the distance between detector and source. However, this method is destructive and may potentially

disturb sediment structures, particularly when extracting 150 cm-long U-channels. In the context of this study, the main priority is to evaluate how well the scans capture a large set of varve boundaries, not study detailed microfacies. The first scanned core section from Lake Sagtjernet revealed that scanning at voxel sizes of 45.5 and 53.0 μm was sufficient to capture varve boundaries well. Additionally, the top meters of the sediments were too wet to extract in U-channels and mount upright without disturbing the sediment. Therefore, we opted against the U-channel method. Although sample length does not have an impact on scanning resolution, the compromise between sample diameter and sample resolution remains one of the main restrictions for μCT imaging of sediments (Bendle et al., 2015).

The file size of uncompressed ~50 μm resolution scans of 150 cm-long sediment cores are currently too large for the μCT system at EARTHLAB to visualize. We therefore tested binning the scans to both ~100 and ~200 μm voxel sizes. Binning gives better contrast and signal-to-noise ratio, however, at the cost of image resolution. The ~100 μm resolution binned scans allow for visualization in *Avizo,* however the performance is slow and does not significantly improve the ability to recognize varve boundaries compared to the ~200 μm resolution binned files. While binning to ~100 μm is beneficial for analysing microstructures of varves, we conclude that it does not provide a sufficient increase in varve detail compared to the loss of visualization performance. To visualize unbinned ~50 μm resolution scans, the core sections would need to be scanned as smaller segments (e.g. 50 cm-length) to reduce the file size. This is a limitation which undoubtedly will be overcome by future advances in computing power.

Given the average VQI of 2.1, the representation of varves in the μCT images is generally good. However, there are stratigraphic variations in how varves are represented in μCT images. Optical images and visual observation of lithology Unit A (0–84 cm depth) shows the presence of varves, however, these are not captured in the μCT scans (Fig. 5.1). A likely explanation for this is the lack of compaction of sediments compared to deeper sediments, which would reduce the density contrast between the two sub-lamina of the varves. High water content in the sediments (>85%) could further reduce the density contrast between varves and make them invisible in the μCT scan. In the varved sequence of the core (Unit B; 84–533 cm), there are smaller intervals (2–10 cm thick) where the varve boundaries in the μCT scans become vague (VQI 0–1; Fig. 8). These intervals correspond to the 'black bands' seen on optical images (e.g. Figs. 5.3 and 5.4). Although the varves also become optically less distinct, they are still discernible. Geochemically the black bands are mainly characterized by a strong reduction in Fe and Mn (e.g. Figs. 5.3 and 5.4). The lower levels of Fe and Mn are likely linked to less precipitation of Fe–Mn hydroxides, which could be caused by prolonged stratification and anoxic bottom water conditions (Makri et al., 2021). When the varves become too indistinct to count in these sections, the support of other methods (e.g. thin sections) can additionally be applied, an argument also supported by Emmanouilidis et al. (2020).

Although this study focuses on the use of μCT scanning to detect boundaries in ferrogenic varves, the method is not limited to this varve type only. The main factor controlling how well varve boundaries can be resolved is sufficient density difference between seasonal lamina. Other common varve types, such as clastic-biogenic varves, likely are even more suited for using μCT to produce varve chronologies due to the strong density difference between the clastic winter lamina and organic summer lamina. Consequently, we wish to highlight the large potential that lies in using μCT to produce varve chronologies in sediment records containing other varve types.

5.4. Comparison of varve counts and independent chronology

As the varves in Lake Sagtjernet cannot confidently be counted continuously to the top of the core, the varve chronology is considered 'floating' and should ideally be anchored by a stratigraphic isochron, such as cryptotephra from volcanic eruptions (Zolitschka et al., 2015). However, obtaining stratigraphic isochrons within the varve counted sequence is outside of the scope of this study. Therefore, we opted to anchor the varve chronology to the uppermost ^{14}C date (Beta-341430) of the varve counted interval. This places the top of the varved sequence at 425 cal. years BP and the bottom at 4460 cal. years BP. This leads the entire varve chronology to fall within the 95% confidence interval of the radiocarbon-based chronology (Fig. 8). The correspondence between the two chronologies strongly supports our argument that the laminations in Lake Sagtjernet indeed are varves.

6. Conclusions

We analysed the sediments of Lake Sagtjernet (Eastern Norway) to explore the processes of varve formation and to quantify the varves using μCT. The 593 cm of sediments cover the past 10274 $^{+220}/_{-329}$ years. Combining limnological monitoring, microfacies analyses and independent age validation, we are able to show that the laminations from 84 to 533 cm depth (75% of the sediment record) are rare ferrogenic varves. A radiocarbon-based age-depth model together with lithological analyses shows that the varves abruptly start forming in Lake Sagtjernet 4548 $^{+132}/_{-117}$ cal. years BP. These varves are composed of two major sub-lamina: (1) a thinner pale lamina composed of Fe and Mn hydroxides deposited during late fall and early spring, and (2) a thicker darker lamina composed of amorphous organic matter deposited during the summer growing-season. This pattern is further reflected in μCT scans as an oscillation between a higher density lamina (coinciding with Fe and Mn maxima in the μXRF scans) and a lower density lamina (coinciding with amorphous organic matter lamina).

In this study, we present the use of μCT scans to construct a floating varve chronology, at scanning resolutions of ~50 μm (binned to ~200 μm) for core sections with lengths up to 150 cm. Overall, varve boundaries are easily determined, although shorter sediment sections reveal less clear varve boundaries where complimentary count techniques (e.g. thin sections) can be helpful to reduce the varve count uncertainty. Furthermore, the 3D nature of μCT scans makes them excel at identifying disturbed sections of sediments that can be taken into account before further analyses of a sediment core. Two sets of varve counts on exported μCT images are combined to produce the first continuous non-glacial varve chronology from a Norwegian lake covering 4023 $^{+113}/_{-185}$ varve years.

Considering the annual resolution of Lake Sagtjernet sediments, we foresee that this record provides a key reference site for future paleoclimatological and paleoenvironmental studies in Scandinavia. Finally, we identify three promising directions for future work: (1) obtaining stratigraphic isochrons in the varved sequence (e.g. cryptotephra) to anchor the varve chronology and reduce the uncertainty of the age-depth model, (2) developing techniques to quantify varves using the full 3D potential of the μCT scans (e.g. machine learning), and (3) dedicated paleoecological and paleoclimatological proxy reconstructions using the high resolution varve chronology of Lake Sagtjernet.

Declaration of competing interest

The authors declare that they have no known competing financial interests or personal relationships that could have appeared to influence the work reported in this paper.

Data availability

Data will be made available on request.

Acknowledgement

This work was funded by the Research Council of Norway through the FRIPRO project VIKINGS (project no. 275191) and supported by the

Centre of Excellence grant to CEED (project no. 223272) at the University of Oslo, and the National infrastructure EARTHLAB (project no. 226171) at the University of Bergen. We thank Jan Magne Cederstrøm for guidance and valuable suggestions on μCT scanning. We thank Irina Maria Dumitru (University of Bergen) and Siri Simonsen (University of Oslo) for their help producing and analysing the thin sections. We thank Kennedy Alexandra Lange for valuable comments on the manuscript. We also thank two anonymous reviewers who provided valuable comments and suggestions that greatly improved the quality of this paper.

Appendix A. Supplementary Data

Supplementary Data to this article can be found online at https://doi.org/10.1016/j.quageo.2023.101432.

References

Anthony, R.S., 1977. Iron-rich rhythmically laminated sediments in Lake of the Clouds, northeastern Minnesota. Limnol. Oceanogr. 22, 45–54. https://doi.org/10.4319/lo.1977.22.1.0045.

Appleby, P.G., 1986. 210Pb dating by low background gamma counting. Hydrobiologia 143, 21–27.

Appleby, P.G., Oldfield, F., 1978. The calculation of lead-210 dates assuming a constant rate of supply of unsupported 210Pb to the sediment. Catena 5, 1–8. https://doi.org/10.1016/S0341-8162(78)80002-2.

Appleby, P.G., Richardson, N., Nolan, P.J., 1991. ^{241}Am dating of lake sediments. Hydrobiologia 214, 35–42.

Appleby, P.G., Richardson, N., Nolan, P.J., 1992. Self-absorption corrections for well-type germanium detectors. Nuclear Instruments and Methods in Physics Research Section B: Beam Interactions with Materials and Atoms 71, 228–233.

Bendle, J.M., Palmer, A.P., Carr, S.J., 2015. A comparison of micro-CT and thin section analysis of Lateglacial glaciolacustrine varves from Glen Roy, Scotland. Quat. Sci. Rev. 114, 61–77. https://doi.org/10.1016/j.quascirev.2015.02.008.

Blaauw, M., Christen, J.A., 2011. Flexible paleoclimate age-depth models using an autoregressive gamma process. Bayesian Anal 6, 457–474. https://doi.org/10.1214/11-BA618.

Boes, E., Van Daele, M., Moernaut, J., Schmidt, S., Jensen, B.J.L., Praet, N., Kaufman, D., Haeussler, P., Loso, M.G., De Batist, M., 2017. Varve formation during the past three centuries in three large proglacial lakes in south-central Alaska. GSA Bull 130, 757–774. https://doi.org/10.1130/B31792.1.

Brauer, A., Haug, G.H., Dulski, P., Sigman, D.M., 2008. An abrupt wind shift in western Europe at the onset of the Younger Dryas cold period. Nat. Geosci. 1, 520–523. https://doi.org/10.1038/ngeo263.

Butz, C., Grosjean, M., Fischer, D., Wunderle, S., Tylmann, W., Rein, B., 2015. Hyperspectral imaging spectroscopy: a promising method for the biogeochemical analysis of lake sediments. J. Appl. Remote Sens. 9, 096031 https://doi.org/10.1117/1.JRS.9.096031.

Christiansen, P.B., Bergaust, O.P., 1991. Fagrapport om Sagtjernet: en analyse av Sagtjernet og dets økosystem. In: Elverum Average Temperature and Average Precipitation. Unpublished report.Climate-data.org, 2022.

Cnudde, V., Boone, M.N., 2013. High-resolution X-ray computed tomography in geosciences: a review of the current technology and applications. Earth Sci. Rev. 123, 1–17. https://doi.org/10.1016/j.earscirev.2013.04.003.

Croudace, I.W., Rothwell, R.G. (Eds.), 2015. Micro-XRF Studies of Sediment Cores: Applications of a Non-destructive Tool for the Environmental Sciences. Springer, Dordrecht, Netherlands.

Davison, W., 1993. Iron and manganese in lakes. Earth Sci. Rev. 34, 119–163. https://doi.org/10.1016/0012-8252(93)90029-7.

Davison, W., Tipping, E., 1984. Treading in Mortimer's footsteps: the geochemical cycling of iron and manganese in Esthwaite Water. Freshw. Biol. Assoc. 91–101.

de Geer, G., 1912. Geochronologie der letzten 12000 Jahre. Geol. Rundsch. 3, 457–471. https://doi.org/10.1007/BF01802565.

Denys, L., 2009. Incomplete spring turnover in small deep lakes in SE Michigan. McNair Sch. Res. J. 2, 133–144.

Duliu, O.G., 1999. Computer axial tomography in geosciences: an overview. Earth Sci. Rev. 48, 265–281. https://doi.org/10.1016/S0012-8252(99)00056-2.

Eikenæs, O., Njøs, A., Østdahl, T., Taugbøl, T., 2000. Flommen kommer: sluttrapport fra HYDRA - et forskningsprogram om flom. Norges vassdrag- og energidirektorat.

Emmanouilidis, A., Messaris, G., Ntzanis, E., Avramidis, P., 2019. Microstructural and facies identification through X-ray computed tomography (CT) on annually laminated sediments. Presented at the 19th International Multidisciplinary Scientific Geoconference SGEM 2019, 7.

Emmanouilidis, A., Unkel, I., Seguin, J., Keklikoglou, K., Gianni, E., Avramidis, P., 2020. Application of non-destructive techniques on a varve sediment record from vouliagmeni coastal lake, eastern gulf of corinth, Greece. Appl. Sci. 10, 8273. https://doi.org/10.3390/app10228273.

Fortin, D., Francus, P., Gebhardt, A.C., Hahn, A., Kliem, P., Lisé-Pronovost, A., Roychowdhury, R., Labrie, J., St-Onge, G., 2013. Destructive and non-destructive density determination: method comparison and evaluation from the Laguna Potrok Aike sedimentary record. Quat. Sci. Rev. 71, 147–153. https://doi.org/10.1016/j.quascirev.2012.08.024.

Fortin, D., Praet, N., McKay, N.P., Kaufman, D.S., Jensen, B.J.L., Haeussler, P.J., Buchanan, C., De Batist, M., 2019. New approach to assessing age uncertainties – the 2300-year varve chronology from Eklutna Lake, Alaska (USA). Quat. Sci. Rev. 203, 90–101. https://doi.org/10.1016/j.quascirev.2018.10.018.

Gunnars, A., Blomqvist, S., Johansson, P., Andersson, C., 2002. Formation of Fe(III) oxyhydroxide colloids in freshwater and brackish seawater, with incorporation of phosphate and calcium. Geochem. Cosmochim. Acta 66, 745–758. https://doi.org/10.1016/S0016-7037(01)00818-3.

Hansen, L., Tassis, G., Høgaas, F., 2020. Sand dunes and valley fills from Preboreal glacial-lake outburst floods in south-eastern Norway – beyond the aeolian paradigm. Sedimentology 67, 810–848. https://doi.org/10.1111/sed.12663.

Høgaas, F., Longva, O., 2018. The late-glacial ice-dammed lake Nedre Glomsjø in Mid-Norway: an open lake system succeeding an actively retreating ice sheet. Nor. J. Geol. 98, 1–15. https://doi.org/10.17850/njg98-4-08.

Høgaas, F., Longva, O., 2016. Mega deposits and erosive features related to the glacial lake Nedre Glomsjø outburst flood, southeastern Norway. Quat. Sci. Rev. 151, 273–291. https://doi.org/10.1016/j.quascirev.2016.09.015.

Høgaas, F., Hansen, L., Berthling, I., Klug, M., Longva, O., Nannestad, H.D., Olsen, L., Romundset, A., 2023. Timing and maximum flood level of the Early Holocene glacial lake Nedre Glomsjø outburst flood, Norway. Boreas.

Hongve, D., 2002. Seasonal mixing and genesis of endogenic meromixis in small lakes in southeast Norway. Nord. Hydrol 33, 189–206. https://doi.org/10.2166/nh.2002.0022.

Hongve, D., 1997. Cycling of iron, manganese, and phosphate in a meromictic lake. Limnol. Oceanogr. 42, 635–647. https://doi.org/10.4319/lo.1997.42.4.0635.

Hongve, D., 1980. Chemical stratification and stability of meromictic lakes in the Upper Romerike district. Schweiz. Z. Hydrol. 42, 171–195. https://doi.org/10.1007/BF02502433.

Hounsfield, G.N., 1973. Computerized transverse axial scanning (tomography): Part 1. Description of system. Br. J. Radiol. 46, 1016–1022. https://doi.org/10.1259/0007-1285-46-552-1016.

Kalskin, R., Hilmo, B.O., 1999. Kartlegging av potensialet for grunnvarmeuttak fra løsmasser i Elverum. Nor. Geol. Unders. Retrieved from. https://openarchive.ngu.no/ngu-xmlui/handle/11250/2665350 68.

Ketcham, R.A., Carlson, W.D., 2001. Acquisition, optimization and interpretation of X-ray computed tomographic imagery: applications to the geosciences. Comput. Geosci. 27, 381–400. https://doi.org/10.1016/S0098-3004(00)00116-3.

Kjensmo, J., 1968. Iron as the primary factor rendering lakes meromictic, and related problems. Mitt Intern. Ver. Limnol 14, 83–93.

Lamoureux, S., 2001. Varve chronology techniques. In: Last, W.M., Smol, J.P. (Eds.), Tracking Environmental Change Using Lake Sediments: Basin Analysis, Coring, and Chronological Techniques, Developments in Paleoenvironmental Research. Springer Netherlands, Dordrecht, pp. 247–260. https://doi.org/10.1007/0-306-47669-X_11.

Lamoureux, S.F., 1994. Embedding unfrozen lake sediments for thin section preparation. J. Paleolimnol. 10, 141–146. https://doi.org/10.1007/BF00682510.

Liu, X., Colman, S.M., Brown, E.T., Minor, E.C., Li, H., 2013. Estimation of carbonate, total organic carbon, and biogenic silica content by FTIR and XRF techniques in lacustrine sediments. J. Paleolimnol. 50, 387–398. https://doi.org/10.1007/s10933-013-9733-7.

Lotter, A.F., Lemcke, G., 1999. Methods for preparing and counting biochemical varves. Boreas 28, 243–252. https://doi.org/10.1111/j.1502-3885.1999.tb00218.x.

Makri, S., Wienhues, G., Bigalke, M., Gilli, A., Rey, F., Tinner, W., Vogel, H., Grosjean, M., 2021. Variations of sedimentary Fe and Mn fractions under changing lake mixing regimes, oxygenation and land surface processes during Late-glacial and Holocene times. Sci. Total Environ. 755, 143418 https://doi.org/10.1016/j.scitotenv.2020.143418.

Montgomery, H.a.C., Thom, N.S., Cockburn, A., 1964. Determination of dissolved oxygen by the winkler method and the solubility of oxygen in pure water and sea water. J. Appl. Chem. 14, 280–296. https://doi.org/10.1002/jctb.5010140704.

Mortimer, C.H., 1941. The exchange of dissolved substances between mud and water in lakes. J. Ecol. 30, 147–201.

Nesje, A., 1992. A piston corer for lacustrine and marine sediments. Arct. Alp. Res. 24, 257–259. https://doi.org/10.1080/00040851.1992.12002956.

Ojala, A.E.K., Francus, P., Zolitschka, B., Besonen, M., Lamoureux, S.F., 2012. Characteristics of sedimentary varve chronologies – a review. Quat. Sci. Rev. 43, 45–60. https://doi.org/10.1016/j.quascirev.2012.04.006.

Oppistov, T.G., 2019. Revurdering Av Beskyttelsessoner Rundt Elverum Vannverk (Master's Thesis. Norwegian University of Life Sciences: NMBU).

Orsi, T.H., Edwards, C.M., Anderson, A.L., 1994. X-ray computed tomography: a nondestructive method for quantitative analysis of sediment cores. J. Sediment. Res. 64.

Papadimitrakis, 2019. An Assessment of Grindalsmoen Aquifer, Elverum, Norway–Field Observations and Groundwater Modeling. Master's thesis, University of Oslo, Norway). Retrieved from. http://urn.nb.no/URN:NBN:no-74246.

Rach, O., Brauer, A., Wilkes, H., Sachse, D., 2014. Delayed hydrological response to Greenland cooling at the onset of the Younger Dryas in western Europe. Nat. Geosci. 7, 109–112. https://doi.org/10.1038/ngeo2053.

Ramsey, C., Reimer, P., Austin, W., Bard, E., 2020. The IntCal20 Northern Hemisphere Radiocarbon Age Calibration Curve (0-55 Kcal BP).

Reimer, P.J., Austin, W.E.N., Bard, E., Bayliss, A., Blackwell, P.G., Bronk Ramsey, C., Butzin, M., Cheng, H., Edwards, R.L., Friedrich, M., Grootes, P.M., Guilderson, T.P., Hajdas, I., Heaton, T.J., Hogg, A.G., Hughen, K.A., Kromer, B., Manning, S.W., Muscheler, R., Palmer, J.G., Pearson, C., van der Plicht, J., Reimer, R.W., Richards, D.A., Scott, E.M., Southon, J.R., Turney, C.S.M., Wacker, L., Adolphi, F., Büntgen, U., Capano, M., Fahrni, S.M., Fogtmann-Schulz, A., Friedrich, R., Köhler, P., Kudsk, S., Miyake, F., Olsen, J., Reinig, F., Sakamoto, M., Sookdeo, A.,

Talamo, S., 2020. The IntCal20 Northern Hemisphere radiocarbon age calibration curve (0-55 kcal BP). Radiocarbon 62, 725–757. https://doi.org/10.1017/RDC.2020.41.

Renberg, I., 1981. Formation, structure and visual appearance of iron-rich, varved lake sediments. Int. Ver. Für Theor. Angew. Limnol. Verhandlungen 21, 94–101.

Swanner, E.D., Lambrecht, N., Wittkop, C., Harding, C., Katsev, S., Torgeson, J., Poulton, S.W., 2020. The biogeochemistry of ferruginous lakes and past ferruginous oceans. Earth Sci. Rev. 211, 103430 https://doi.org/10.1016/j.earscirev.2020.103430.

van der Bilt, W.G.M., Cederstrøm, J.M., Støren, E.W.N., Berben, S.M.P., Rutledal, S., 2021. Rapid tephra identification in geological archives with computed tomography: experimental results and natural applications. Front. Earth Sci. 8, 622386 https://doi.org/10.3389/feart.2020.622386.

Vandergoes, M.J., Howarth, J.D., Dunbar, G.B., Turnbull, J.C., Roop, H.A., Levy, R.H., Li, X., Prior, C., Norris, M., Keller, L.D., Baisden, W.T., Ditchburn, R., Fitzsimons, S. J., Bronk Ramsey, C., 2018. Integrating chronological uncertainties for annually laminated lake sediments using layer counting, independent chronologies and Bayesian age modelling (Lake Ohau, South Island, New Zealand). Quat. Sci. Rev. 188, 104–120. https://doi.org/10.1016/j.quascirev.2018.03.015.

Wittkop, C., Teranes, J., Lubenow, B., Dean, W.E., 2014. Carbon- and oxygen-stable isotopic signatures of methanogenesis, temperature, and water column stratification in Holocene siderite varves. Chem. Geol. 389, 153–166. https://doi.org/10.1016/j.chemgeo.2014.09.016.

Woodward, C.A., Gadd, P.S., 2019. The potential power and pitfalls of using the X-ray fluorescence molybdenum incoherent: coherent scattering ratio as a proxy for sediment organic content. Quat. Int. https://doi.org/10.1016/j.quaint.2018.11.031.

Zolitschka, B., Francus, P., Ojala, A.E.K., Schimmelmann, A., 2015. Varves in lake sediments – a review. Quat. Sci. Rev. 117, 1–41. https://doi.org/10.1016/j.quascirev.2015.03.019.

Zolitschka, B., Polgar, I.S., Behling, H., 2022. Created by the Monte Peron rock avalanche: lago di Vedana (Dolomites, Italy) and its sediment record of landscape evolution after a mass wasting event. Landslides 19, 297–311. https://doi.org/10.1007/s10346-021-01787-2.